CrossMark click for updates

PHYSICS OF FLUIDS **28**, 056601 (2016)

Influence of anisotropic permeability on convection in porous media: Implications for geological CO_2 sequestration

Marco De Paoli,[1,2,a)] Francesco Zonta,[1,2,b)] and Alfredo Soldati[1,2,3,c)]
[1]*Department of Electrical, Management and Mechanical Engineering, University of Udine, Udine 33100, Italy*
[2]*Institute of Fluid Mechanics and Heat Transfer, Technische Universität Wien, 1060 Wien, Austria*
[3]*Department of Fluid Mechanics, CISM, Udine 33100, Italy*

(Received 18 December 2015; accepted 9 April 2016; published online 2 May 2016)

Solute convection in porous media at high Rayleigh-Darcy numbers has important fundamental features and may also bear implications for geological CO_2 sequestration processes. With the aid of direct numerical simulations, we examine the role of anisotropic permeability on the distribution of solutal concentration in fluid saturated porous medium. Our computational analyses span over few decades of Rayleigh-Darcy number and confirm the linear scaling of Nusselt number that was previously found in the literature. In addition, we find that anisotropic permeability $\gamma < 1$, i.e., with vertical permeability smaller than horizontal permeability, effectively increases the Nusselt number compared with isotropic conditions. We link this seemingly counterintuitive effect with the occurring modifications to the flow topology in the anisotropic conditions. Finally, we use our data computed for the two-sided configuration (i.e., Dirichlet conditions on upper and lower boundaries) to examine the time evolution of solutal dynamics in the one-sided configuration, and we demonstrate that the finite-time (short-term) amount of CO_2 that can be dissolved in anisotropic sedimentary rocks is much larger than in isotropic rocks. *Published by AIP Publishing.* [http://dx.doi.org/10.1063/1.4947425]

I. INTRODUCTION

When a temperature difference is applied to a liquid filled porous layer, buoyancy driven flows may arise. If we refer to a two-dimensional cartesian layer across which a small temperature difference is applied, the arising gravity driven flow is dominated by diffusion. When temperature increases, instabilities occur and the flow becomes unstable and chaotic, finally achieving a fully convective regime. The temperature difference driving the flow within the layer is represented by a suitable dimensionless number, called the Rayleigh-Darcy number Ra, which quantifies the relative importance of advection compared to diffusion. Archival literature in this field is focused mainly on the onset of instabilities, which occurs[1,2] at $Ra = 4\pi^2$. The flow transfer efficiency is measured in terms of the Nusselt number (Nu), which supplies the value of the dimensionless heat flux transferred across the boundaries of the system. For the case of practical interest at large Rayleigh-Darcy numbers (up to $Ra = 4 \times 10^4$), it was shown by Hewitt *et al.*[3] that Nu increases almost linearly with Ra, in good agreement with previous numerical and experimental studies.[4,5] The above-mentioned problem maintains the same mathematical description when a solute difference is applied across the layer. In this case, the driving parameter is a modified version of the Rayleigh-Darcy number Ra based on the concentration difference and the flow of solute is parametrized by the Sherwood number (Sh) or, more frequently, by a modified Nusselt number based on the concentration gradient.

a)Email: depaoli.marco@spes.uniud.it
b)Email: francesco.zonta@uniud.it
c)Author to whom correspondence should be addressed. Electronic mail: soldati@uniud.it

The literature on this problem is vast and old, dating back to the Darcy's work for the derivation of the governing equations. However, in recent years this problem has received renovated attention for the implications it can bear in carbon dioxide (CO_2) sequestration strategies.[6,7] With reference to this problem, sequestration of liquid CO_2 via injection into brine-filled large geological formations has been identified as one of the possible remedies.[8–10] Essential aspects of CO_2 capture mechanisms are as follows: after injection, CO_2 dissolves in the brine (3% in weight), forms a heavier solute (CO_2 + brine), and flows downward. An accurate evaluation of the solute downward flux is crucial to determine the filling time of the available reservoir capacity (from 320 to 10 000 Gt worldwide, see Xu *et al.*[11]), and consequently the optimal rate of CO_2 injection beneath the earth surface. However, the geological scale *Ra* numbers are of the order of 10^4–10^5, which makes precise flow predictions hard to obtain.

According to current modelling approaches,[3,4] the archetypal system to study solute convection into sedimentary rocks is the two-sided Rayleigh-Bénard configuration in which convective transport occurs between a lighter layer (lower boundary) and a heavier layer (upper boundary). An alternative approach, perhaps more related to the physics of the concentration driven CO_2 dissolution process, is the so-called one-sided configuration.[12,13] In the one-sided configuration, convective transport occurs only away from the upper boundary and the dynamics of the system is a function of time. After onset, heavy plumes fall vertically with possible minor sideway perturbations, which in turn may produce plume interactions and branching before impingement on the lower boundary. Due to the impermeable bottom boundary condition, the domain starts filling up with dense solute and vertical convection is hindered (shutdown).

Even though sedimentary geological formations, which are composed of the subsequent deposition of horizontal layers, are inherently anisotropic[11] and are characterized by different values of the vertical-to-horizontal permeability ratio ($\gamma = K_v/K_h$), estimates for the vertical flux of solute (Nu) in the literature[3,4,14] are almost entirely based on the assumption of isotropic media ($\gamma = 1$). To date, there are only few works[11,15,16] on solute convection in anisotropic porous media, which however mainly focused on the study of instability inception, characterized by *Ra* lower than those typical of geological CO_2 sequestration. Our aim here is to explore the role of the anisotropic rock permeability (different values of γ) and to extend previous analyses on solute convection at large Rayleigh-Darcy numbers in anisotropic porous media.

The paper is built as follows. In Sec. II, we will describe the governing equations and the boundary conditions adopted to run the present numerical simulations. We will consider first the analysis of the two-sided configuration: since in this configuration the flow reaches a steady state dynamic, time averages can be done and can help to identify the main convection mechanisms in a more convincing way if compared with the one-sided configuration.[7] Also important is that the dissolution flux of solute in the one-sided cell can be directly computed from the two-sided model.[12] In Sec. III, we will discuss the role of the anisotropic rock permeability on the vertical flux of solute. In particular, we will show that, compared to the isotropic case, increasing the horizontal rock permeability leads to a remarkably larger downward flux of solute. A physical explanation of this result will be also given based on a detailed examination of the flow topology. In Sec. IV, we will use our previous results on the two-sided configuration to introduce and discuss the dynamics of the one-sided configuration. We generalize the shutdown model presented in the literature,[12] accounting for the influence of the anisotropic rock permeability on the overall amount of solute dissolved in time. Finally, we will draw conclusions on possible implications of our results on long-term CO_2 storage.

II. METHODOLOGY

We consider a fluid-saturated porous medium in a two dimensional domain, assuming a uniform porosity ϕ and considering different values of the vertical (K_v) to horizontal (K_h) permeability ratio $0.25 \leq \gamma \leq 1$. The value of $\gamma < 1$ is chosen to be representative of real geological applications,[16] i.e., $\gamma < 1$. The unstable density stratification (characterized by a top-to-bottom density difference $\Delta\rho^*$) drives the solute in a downward flow which is incompressible and governed by

the Darcy's law. In a two dimensional domain, being u^* and w^* the velocities along the horizontal (x^*) and the vertical directions (z^*), respectively, and with p^* and C^* the pressure and solute concentrations, the balance equations are

$$\frac{\mu}{K_h}u^* = -\frac{\partial p^*}{\partial x^*} \quad , \quad \frac{\mu}{K_v}w^* = -\frac{\partial p^*}{\partial z^*} - \rho^* g, \tag{1}$$

$$\frac{\partial u^*}{\partial x^*} + \frac{\partial w^*}{\partial z^*} = 0, \tag{2}$$

where μ is the fluid viscosity and g the acceleration due to gravity. The superscript $*$ denotes dimensional variables. For the range of Rayleigh numbers considered in the present study, the Oberbeck-Boussinesq hypothesis could be applied.[17] As a consequence, we assume that the fluid density ρ^* is the only solute-dependent property, which can be evaluated in terms of the concentration of solute C^* into the mixture using the linear equation of state,

$$\rho^* = \rho_s^*\left[1 - a(C_s^* - C^*)\right], \tag{3}$$

where a is a positive constant coefficient while C_s^* and ρ_s^* are the concentration field and the density value at the top boundary.

Neglecting the effects of dispersion, and indicating with D the solute diffusivity, the concentration fulfills the time-dependent advection-diffusion equation,

$$\phi\frac{\partial C^*}{\partial t^*} + u^*\frac{\partial C^*}{\partial x^*} + w^*\frac{\partial C^*}{\partial z^*} = \phi D\left(\frac{\partial^2 C^*}{\partial x^{*2}} + \frac{\partial^2 C^*}{\partial z^{*2}}\right). \tag{4}$$

We assume impenetrable boundaries kept at a fixed solute concentration (mimicking the presence of a saturated solution near the top boundary and of pure fluid near the bottom boundary),

$$w^* = 0, \quad C^* = 0 \quad \text{on} \quad z^* = 0, \tag{5}$$

$$w^* = 0, \quad C^* = C_s^* \quad \text{on} \quad z^* = H^*, \tag{6}$$

whereas periodicity is applied along the horizontal direction x^*.

A. Dimensionless equations

A relevant velocity scale for the flow is the free-fall buoyancy velocity, $W^* = gK_v\Delta\rho^*/\mu$. To account for the effect of anisotropy, we use different velocity/length scales in the vertical and horizontal directions (through the introduction of the scaling factor $\sqrt{\gamma}$). In particular, we set:

$$x = \frac{x^*}{H/\sqrt{\gamma}}, \quad z = \frac{z^*}{H}, \quad u = \frac{u^*}{W^*/\sqrt{\gamma}}, \quad w = \frac{w^*}{W^*} \tag{7}$$

$$p = \frac{p^*}{\mu W^* H^*/K_v}, \quad C = \frac{C^* - C_s^*}{C_s^*}, \quad t = \frac{t^*}{\phi H^*/W^*}. \tag{8}$$

The governing parameter of the problem is the Rayleigh-Darcy number,

$$Ra = Ra_T \cdot Da = \frac{gH^* K_v \Delta\rho^*}{\mu\phi D}, \tag{9}$$

defined based on the thermal Rayleigh number ($Ra_T = g\Delta\rho^* H^{*3}/\mu D$) and on the Darcy number ($Da = K_v/H^{*2}$). The Rayleigh-Darcy number can also be seen as the ratio of diffusive and convective time scales (but also as an inverse diffusivity[18] or as the dimensionless layer thickness[13]). In dimensionless form, Eqs. (1), (2), and (4) become

$$u = -\frac{\partial P}{\partial x}, \quad w = -\frac{\partial P}{\partial z} - C, \tag{10}$$

$$\frac{\partial u}{\partial x} + \frac{\partial w}{\partial z} = 0, \tag{11}$$

$$\frac{\partial C}{\partial t} + u\frac{\partial C}{\partial x} + w\frac{\partial C}{\partial z} = \frac{1}{Ra}\left(\gamma\frac{\partial^2 C}{\partial x^2} + \frac{\partial^2 C}{\partial z^2}\right), \tag{12}$$

where $P = p + z/(aC_s^*)$ is the reduced pressure. The effect of anisotropy (γ) is explicit only in Eq. (12) but it is also present in the other equations through the reference length/velocity scales defined above. The dimensionless boundary conditions result as follows:

$$w = 0, \quad C = -1 \quad \text{on} \quad z = 0, \tag{13}$$

$$w = 0, \quad C = 0 \quad \text{on} \quad z = 1. \tag{14}$$

Equations (10)-(12) are solved by a Fourier-Chebyshev pseudo-spectral method. Further details on the numerical approach can be found in the Appendix and in the work of Zonta and Soldati.[19]

In the present study, $\gamma < 1$ is obtained by increasing the horizontal permeability K_h while keeping K_v constant (i.e., keeping the same Ra). By doing so, we can compare simulations at the same Ra (i.e., same driving force or same domain height), but different γ (i.e., different porous medium). We perform a systematic study of solutal convection in anisotropic porous media in the Ra parameter space covering a broad range of Ra numbers ($50 \le Ra \le 5 \times 10^4$), while assuming $0.25 \le \gamma \le 1.00$.

III. RESULTS

In this section, we describe the results obtained from numerical simulations of the two-sided configuration with anisotropic rock permeability $\gamma \le 1$. In fact, we start our analysis considering the dynamics of the flow for $\gamma = 1$ (isotropic rock permeability). The dynamics of the present system depends on the value of the Rayleigh-Darcy number. For $Ra \le 4\pi^2$, diffusion dominates and convection is prevented.[1,2] For $4\pi^2 < Ra < 1300$, the flow exhibits large and steady non-linear rolls, with the onset of a secondary instability as Ra approaches the value $Ra \simeq 1300$. This dynamics has been extensively analyzed in previous papers[4,20] and will not be discussed further here. For $Ra > 1300$, the system cannot sustain the stable quasi-periodic configuration and undergoes a transition towards a chaotic state, characterized by the occurrence of unsteady motions.[4]

We describe the flow structure using contour maps of the concentration field C, since concentration is transported by the velocity field and reproduces faithfully the underlying flow structure. The basic fluid mechanics of such flow is depicted in Fig. 1.

We focus on the first row of Fig. 1, which shows contour maps of C in the x–z plane for $Ra = 8 \times 10^3$ (Fig. 1(a)), $Ra = 16 \times 10^3$ (Fig. 1(b)) and $Ra = 5 \times 10^4$ (Fig. 1(c)).

Small fingers of light fluid raise from the bottom boundary moving upward, while corresponding fingers of heavy fluid move downward from the top boundary. These fingers, named *protoplumes* in the work of Hewitt *et al.*,[3] come close each other and form larger plumes (*megaplumes*) that penetrate across the domain and reach the opposite boundary. Large plumes, whose velocity is initially low, are vigorously accelerated by buoyancy and reach the opposite boundary, where they are deflected horizontally. These horizontal branches push closer the newly forming fingers so to produce a new descending (or ascending) large plume in a cyclic fashion.

To further clarify the dynamics of merging plumes, in Figs. 1(d)–1(i), we show the time evolution of the concentration field C measured along an horizontal slice at two different vertical positions. The horizontal slice is located at a distance $z = 10^2/Ra$ from the lower boundary (just outside of the boundary layer) in Figs. 1(d)–1(f), and at $z = 1/2$ (cell centerline) in Figs. 1(g)–1(i). The position of the two cutting planes is explicitly shown in Figs. 1(a)–1(c) and is indicated as z_A, z_B. Near the wall (Figs. 1(d)–1(f)), the emerging picture indicates the presence of a characteristic structure, consisting of protoplumes (small ribs) that coalesce to form megaplumes (long and persistent roots). Adjacent megaplumes can merge or form branches, as indicated by the meandering concentration pattern. From a comparative analysis of Figs. 1(d)–1(f) it is apparent that the number and the strength of protoplumes near the boundary increases with increasing Ra. Farther from the wall (Figs. 1(g)–1(i)), megaplumes increase persistence and stability for increasing Ra. This is revealed by the regular streaky pattern at $Ra = 5 \times 10^4$ (Fig. 1(i)) in comparison with those at smaller Ra (Figs. 1(g) and 1(h)).

The dynamics of protoplumes and megaplumes qualitatively described above for $\gamma = 1$ remains substantially unchanged also for $\gamma \neq 1$, though the assumption of a anisotropic rock permeability produces quantitative effects. To quantify these effects, we consider the behaviour of the

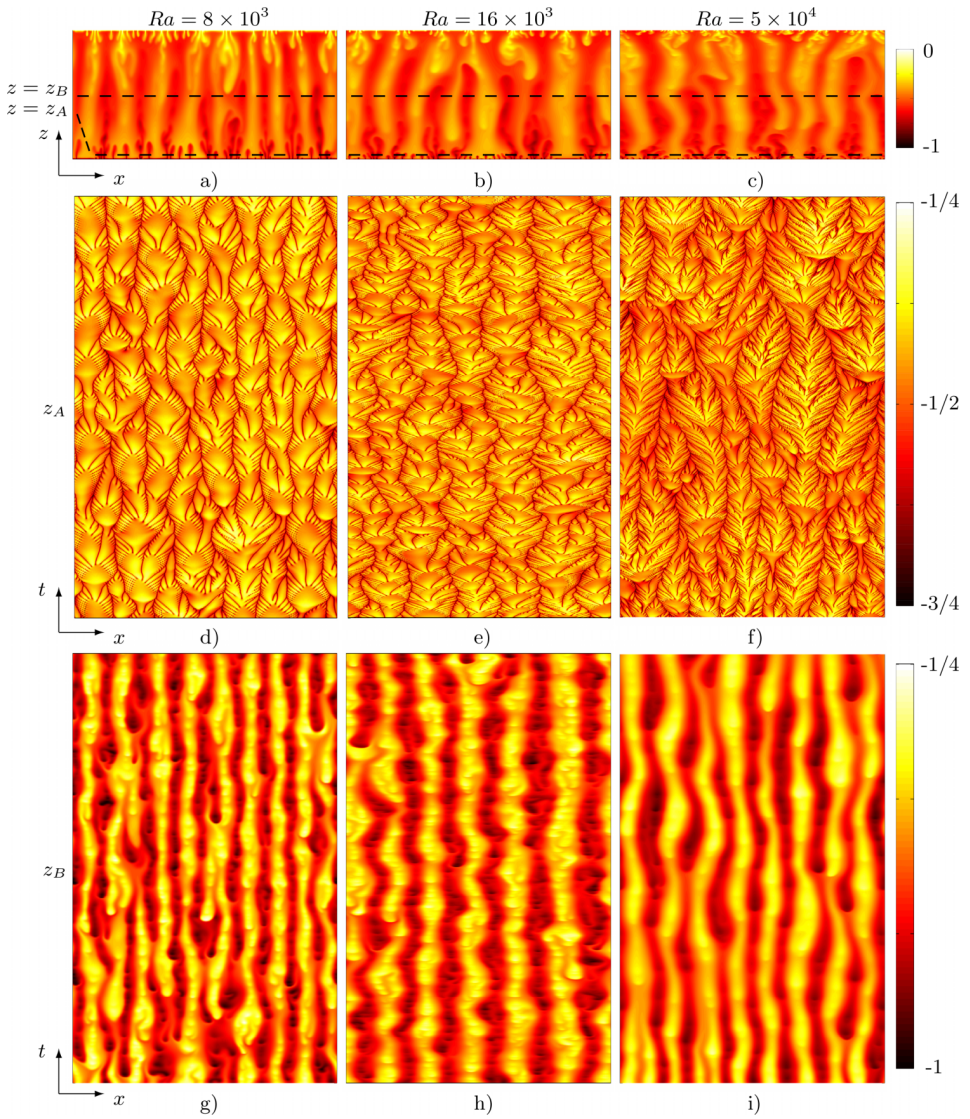

FIG. 1. (a)–(c): contour maps of the concentration field C of the solute for $Ra = 8\times10^3$ (a), $Ra = 16\times10^3$ (b), and $Ra = 5\times10^4$ (c). (d)–(i): space-time measurements of C along two horizontal slices located at $10^2/Ra$ from the lower layer (z_A) (d)–(f), i.e., just outside of the boundary layer whose extension is $15/Ra$, as suggested by Otero *et al.*,[4] and at the centerline of the cell (z_B) (d)–(f). The location of the "cutting planes" z_A and z_B is explicitly shown in (a)–(c). The value of Ra for the space-time measurements corresponds to that of the contour maps in the above panels ($Ra = 8\times10^3$, $Ra = 16\times10^3$ and $Ra = 5\times10^4$ from left to right).

mean concentration profile $\langle C\rangle$ along the vertical direction z. Results are shown in Fig. 2. In particular, in Fig. 2(a) we present the reference results obtained assuming $\gamma = 1$ and varying Ra ($Ra = 8\times10^3$, $Ra = 16\times10^3$ and $Ra = 5\times10^4$). In Fig. 2(b) we show the results obtained for a given Ra ($Ra = 8\times10^3$) and different γ ($\gamma = 1.00$, $\gamma = 0.50$ and $\gamma = 0.25$). Note that brackets $\langle\cdot\rangle$ indicate average in time and in space over the horizontal direction x. A close up view of the mean concentration profiles near the boundary (up to $z = 1/20$) is shown in the inset of each panel. We analyze first the effect of Ra on the mean concentration profile (Fig. 2(a)). The jump of $\langle C\rangle$ to the centerline value $\langle C\rangle = -1/2$ is observed across a thin boundary layer, the thickness of which can be computed as $\delta = \Delta C/2[\partial\langle C\rangle/\partial z]_{z=0} = 1/2[\partial\langle C\rangle/\partial z]_{z=0}$, with ΔC being the overall top-to-bottom concentration difference and equal to 1 due to the concentration scale used. A similar behaviour is also observed for varying γ (Fig. 2(b)). Note that the significant reduction of δ for decreasing γ is a strong indication for the enhanced vertical flux of solute.[21]

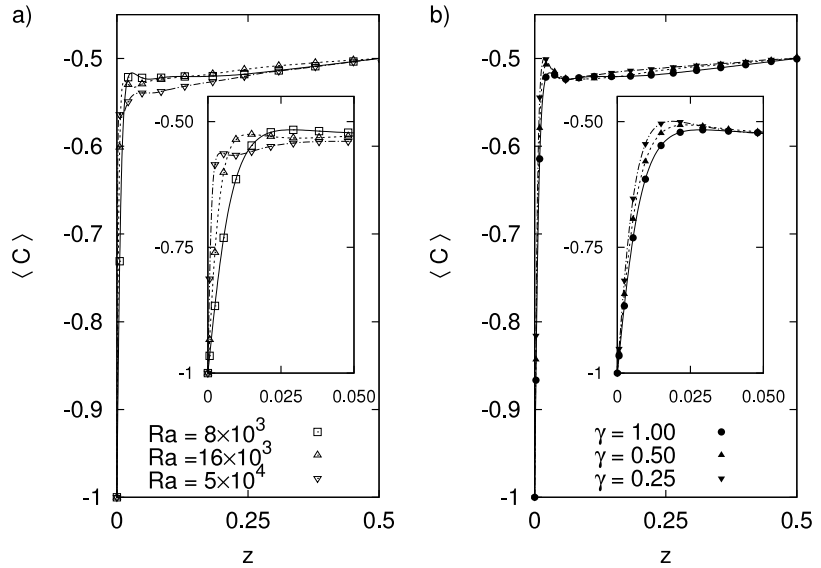

FIG. 2. (a): profiles of the average concentration $\langle C \rangle$ computed along the vertical direction z for different Ra numbers with $\gamma = 1$. (b): profiles of the average concentration $\langle C \rangle$ computed along the vertical direction z at $Ra = 8 \times 10^3$ and different values of γ. The insets in each panel show a close-up view of the region near the boundary.

We briefly discuss here the behaviour of the root mean square (rms) of the solute concentration fluctuations C_{rms} as a function of the vertical coordinate z. Results are shown in Fig. 3. We consider first the effect of Ra on C_{rms} for an isotropic porous medium (Fig. 3(a)). We clearly observe that for increasing Ra the peak of C_{rms} moves toward the boundary while remaining almost constant in amplitude. This is a further indication of the reduction of the boundary layer thickness discussed above. A similar trend is observed for varying γ (Fig. 3(b)). A close up view of the behaviour of C_{rms} near the boundary (up to $z = 1/20$) is provided in the inset of both Figs. 3(a) and 3(b) to

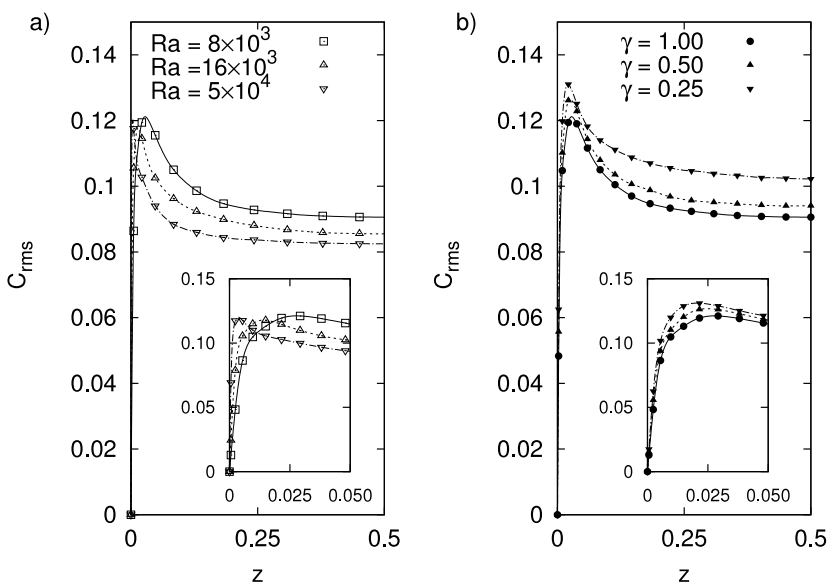

FIG. 3. (a): profiles of the root mean square of the concentration fluctuations, C_{rms}, computed along the vertical direction z for different Ra ($Ra = 8 \times 10^3$, $Ra = 16 \times 10^3$, $Ra = 5 \times 10^4$) and $\gamma = 1$. (b): profiles of the root mean square of the concentration fluctuations computed along the vertical direction z at $Ra = 8 \times 10^3$ and different values of γ ($\gamma = 1$, $\gamma = 0.50$ and $\gamma = 0.25$). The inset in each panel shows a close up view of the region near the boundary.

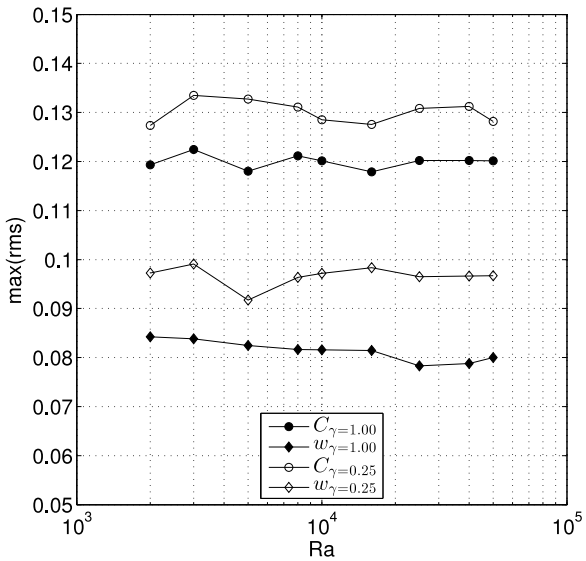

FIG. 4. Maximum value of the temporally and spatially averaged root mean square of the concentration fluctuations (C_{rms}), vertical velocity (w_{rms}) and horizontal velocity (u_{rms}) as a function of Ra and for two values of γ ($\gamma = 1$ and $\gamma = 0.25$).

properly visualize the shape of the C_{rms} profile. The behaviour of the maximum value of solute fluctuations, $\max(rms)$, as a function of Ra and γ is shown in Fig. 4. These results clearly indicate that the maximum value of C_{rms} (as well as of w_{rms}) remains almost constant for increasing Ra. Yet, $\max(C_{rms})$ and $\max(w_{rms})$ increase remarkably for decreasing γ.

To evaluate explicitly the downward solute flux for different Ra, we computed the actual value of the Nusselt number (see the Appendix). The behaviour of Nu as a function of Ra is shown in Fig. 5. The inset refers to the behaviour of Nu over the entire range of Rayleigh numbers simulated in the present work ($50 < Ra < 5 \times 10^4$) for the isotropic porous medium ($\gamma = 1$, $-\circ-$). These

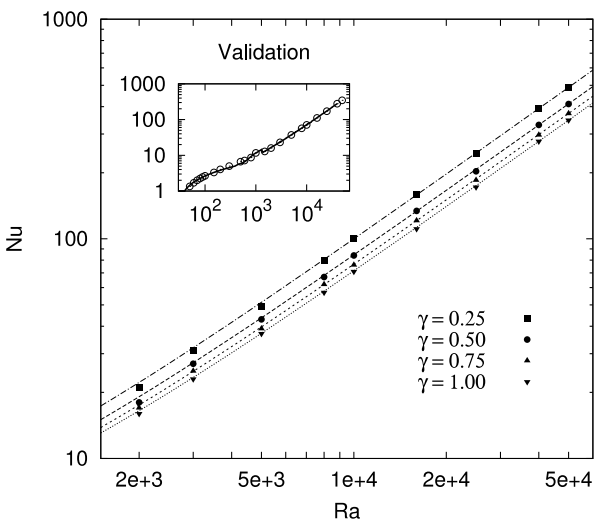

FIG. 5. Time and space averaged Nusselt number Nu as a function of the Rayleigh-Darcy number (Ra) for different values of the permeability ratio $\gamma = K_v/K_h$ ($\gamma = 1$, $\gamma = 0.75$, $\gamma = 0.50$, and $\gamma = 0.25$). Results are shown only for high Rayleigh-Darcy numbers ($Ra \geq 2 \times 10^3$). Predictions from the simplified model $Nu = \beta + \alpha\gamma^n Ra$ (with $\alpha = 0.006\,88$ and $\beta = 2.75$ proposed by Hewitt *et al.*[3] for the isotropic case, and $n = -1/4$ to account for anisotropic permeability) are shown (lines) together with the numerical results (symbols). The inset shows the values of Nu (symbols) for $\gamma = 1$ and for all Ra considered in this study. Results from Hewitt *et al.*[3] (solid line) are also shown for comparison.

results are shown together with those provided by Hewitt *et al.*[3] (—) to confirm and extend previous predictions on the asymptotic linear increase of Nu with Ra.[3,4]

The results shown in the main panel of Fig. 5 are one of the key messages of the present paper. Symbols indicate the values of Nu obtained from simulations at $Ra \geq 2 \times 10^3$ for different γ: $\gamma = 1$ ($-\blacktriangledown-$), $\gamma = 0.75$ ($-\blacktriangle-$), $\gamma = 0.50$ ($-\bullet-$), and $\gamma = 0.25$ ($-\blacksquare-$). A remarkable effect of γ on Nu is easy to observe over the entire range of Ra, with increments of Nu up to about 40% for $\gamma = 0.25$. This provides a clear indication of the enhanced downward flux of solute occurring when increasing the horizontal permeability. We wish to remark here that our simulations for $\gamma < 1$ are run by increasing K_h (horizontal permeability) while keeping K_v (vertical permeability) constant. This choice was necessary to compare our results against previous works[3,4] (we kept Ra constant while varying γ). Current results can be predicted by the linear scaling,

$$Nu = \beta + \alpha \gamma^n Ra, \tag{15}$$

with $\alpha = 0.006\,88$ and $\beta = 2.75$, which extends that proposed by Hewitt *et al.*[3] for the isotropic case $\gamma = 1$: our data show that it is possible to maintain the same scaling, though introducing the permeability ratio γ to the power $-1/4$. Note that the precise value of n obtained from data fitting is $n = -0.2514 \pm 0.0053$. It was not possible to compare our data against previous experimental or numerical results from the literature: we were able to find only few studies[11,15,22] analysing flow convection in a fluid saturated anisotropic porous medium. In the work of Xu *et al.*,[11] the authors studied by linear and global stability analysis the onset of convection (which occurs at lower Ra than those considered here) and found indications that reducing γ leads to a faster solute dissolution (increase of Nu). Later, Cheng *et al.*[15] combined stability analysis and numerical simulations (up to $Ra = 6400$) to show that solutal convection can be triggered earlier in anisotropic porous media, leading the authors to the conclusions that a wider range of potential reservoirs can be effectively exploited for CO_2 sequestration. More recently, Green and Ennis-King[22] found that reducing γ could decrease Nu, which is only in apparent contradiction with our results. In Green and Ennis-King,[22] decreasing γ is obtained by decreasing K_v rather than by increasing K_h. Note however that varying K_v leads to different Ra. Hence, it is difficult to compare results of Nu for different γ (and also different Ra). To the best of our knowledge, these calculations have never been performed in the high-Ra regime. In the following, we will also give sound physical reasons why reducing γ can lead to a seemingly counterintuitive increase of solute vertical flux (Nu).

In the high-Ra regime, the flow is made of a sequence of falling plumes that drive the heavy fluid (high concentration of solute) downward and by rising plumes that drive light fluid (low concentration of solute) upward.[23] In Fig. 6 we show a close up of a falling plume that is developing near the top boundary over a length of one third of the domain. The thick black line identifies the mid-value of the dimensionless concentration $C = -1/2$ and represents the contour of the plume. The values of the vertical velocity gradient, $\partial w/\partial z$, are indicated in Fig. 6(a) with the color range, white being the maximum positive gradient and black being the maximum negative gradient. The values of the vertical velocity, w, are indicated in Fig. 6(b) with the color range, white being the maximum upward velocity and black being the maximum downward velocity. In both Figs. 6(a) and 6(b), flow streamlines are also plotted to show in detail the flow behaviour inside and outside the plume. Focusing on the tiny region near the top boundary (i.e., $z \geq 0.95$ in Fig. 6(a)), it is possible to observe a number of small, concentrated bursts of positive vertical velocity gradient that control the development of the plumes (identified by regions of large downward velocity in Fig. 6(b)). Following the plume structure, we can see that farther from the top boundary ($z \simeq 0.75$) the vertical velocity gradient is small (Fig. 6(a)), indicating that the vertical downward velocity of plumes is maximum (Fig. 6(b)). Flow streamlines clearly mark the regions where the fluid is recirculating due to the shear produced by the falling plume interacting with the neighbouring rising plumes. In an effort to explain the importance of the permeability ratio γ in modifying the flow, we want to focus specifically on the modification to w and $\partial w/\partial z$. We compute the probability density function (PDF) of w and $\partial w/\partial z$ in the region of the falling plumes, as identified in Fig. 6, for different values of γ. We plot the $PDF(\partial w/\partial z)$ in Fig. 7(a) and the $PDF(w)$ in Fig. 7(b). All data are normalized by the corresponding root mean square (rms) for $\gamma = 1$. We discuss first the $PDF(\partial w/\partial z)$ in the

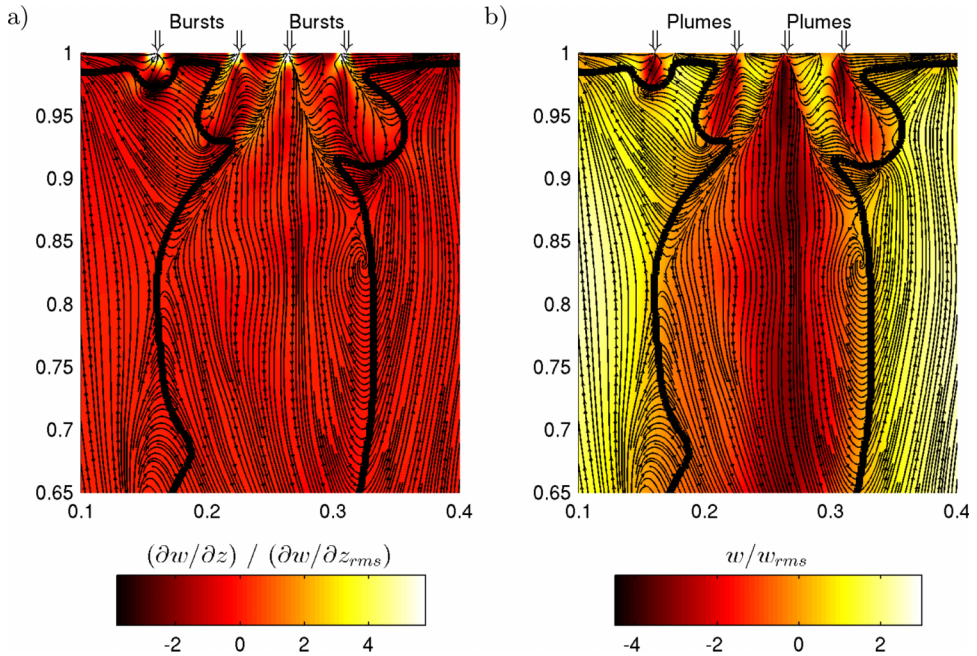

FIG. 6. Sketch of a falling plume near the top boundary, identified by the isocontour $C = -1/2$ (thick line). (a): contour maps of the vertical velocity gradient $\partial w/\partial z$ within the plume, normalized by the root mean square value $\partial w/\partial z_{rms}$. (b): contour maps of the vertical velocity w within the plume, normalized by the root mean square value w_{rms}.

isotropic case, corresponding to $\gamma = 1$ (−■−). The distribution is asymmetric, due to the sampling on the falling plume, with the most probable value in zero. We also observe a wide positive tail, indicating that a large proportion of the events correspond to a velocity increase while the fluid is falling. When γ is decreased, the distribution broadens, demonstrating a more probable occurrence of the positive, but also negative, extreme events. We remark here that while $\partial w/\partial z > 0$ is an indication of plume acceleration, $\partial w/\partial z < 0$ is an indication of plume deceleration. A vis-a-vis comparison of Figs. 6(a) and 7(a) suggests that the events $\partial w/\partial z > 5$, for which we report an

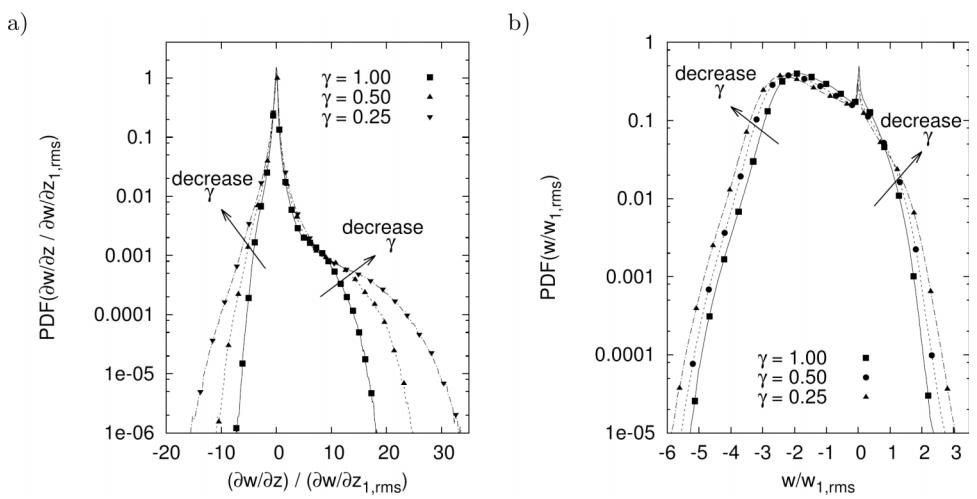

FIG. 7. (a) Probability Density Function (PDF) of the vertical velocity gradient $\partial w/\partial z$, normalized by the root mean square value of $\partial w/\partial z$ for $\gamma = 1$, $\partial w/\partial z_{1,rms}$. (b) Probability Density Function (PDF) of fluid vertical velocity w, normalized by the root mean square value of w for $\gamma = 1$, $w_{1,rms}$. The PDF calculation is done considering only the fluid region of falling plumes (i.e., $C > -1/2$, see Fig. 6). Results refer to the case of $Ra = 8 \times 10^3$.

increase for decreasing γ, are those associated to the newly forming plumes. If we focus on the negative tail, we can associate the increase of events $\partial w/\partial z < -5$ with strong deceleration in the vertical direction of the falling plume when approaching the bottom boundary (not shown in Fig. 6). The decrease of γ has a similar effect also on the distribution of w (Fig. 7(b)): decreasing γ increases the frequency of positive and negative extreme events (predominantly occurring in the core of the plume, see Fig. 6(b)). We report also a decrease of the frequency of moderate events. Falling plumes are large convective regions that entrain the fluid downward. However, falling plumes can exhibit, due to the shearing action of the neighbouring rising plumes, also small areas characterized by lumps of fluid going upward: this explains the positive values in Fig. 7(b). From the qualitative behaviour of Fig. 6 and the quantitative results in Fig. 7, we can now explain why in Fig. 5 we observe an increase of Nu for a decrease of the permeability ratio γ. When we increase the horizontal permeability K_h, we facilitate the horizontal motion of the fluid with a corresponding increase of $\partial u/\partial x$. To preserve the mass balance in the flow domain, continuity must prescribe a corresponding increase of the magnitude of $\partial w/\partial z$. This observation and the broadening of the tails in the velocity distribution reported in Fig. 7(b) can lead us to the conclusion that a decrease of the horizontal resistance induces an increase of the flow in the vertical direction, even though the vertical permeability K_v is maintained constant.

A. Plume dynamics

As discussed above, solute convection in porous media is essentially driven by plumes. For this reason, we wish to investigate further the characteristics of plumes for varying Ra and γ.

1. Plume detection

Plume identification is a longstanding problem in buoyancy-driven flows (see the work of Paparella and von Hardenberg,[24] Ching *et al.*,[25] van der Poel *et al.*,[26] and references therein). Plumes are usually identified based on the value of the velocity-temperature (or concentration) correlation or on the value of the temperature (or concentration) fluctuations. Although the definition of plumes based on these markers leads to slightly different results for pure fluid thermal (or solutal) convection, we checked that in the present case of solutal convection in porous media they all lead essentially to the same results. Following the work of Otero *et al.*,[4] Hewitt *et al.*,[3] and Slim,[13] in the present work, we identify an ascending plume P as the set of points $\mathbf{x} = (x, z)$ (in the domain D), where

$$P = \{\mathbf{x} \in D \quad : \quad C(\mathbf{x}) \geq -1/2\}.$$

An example of plume detection is given in Fig. 8, where we show the contour maps of the concentration field (Fig. 8(a)) and the corresponding shape of plumes detected with the present algorithm, i.e., by detecting the contour line $C(\mathbf{x}) = -1/2$ (Fig. 8(b)).

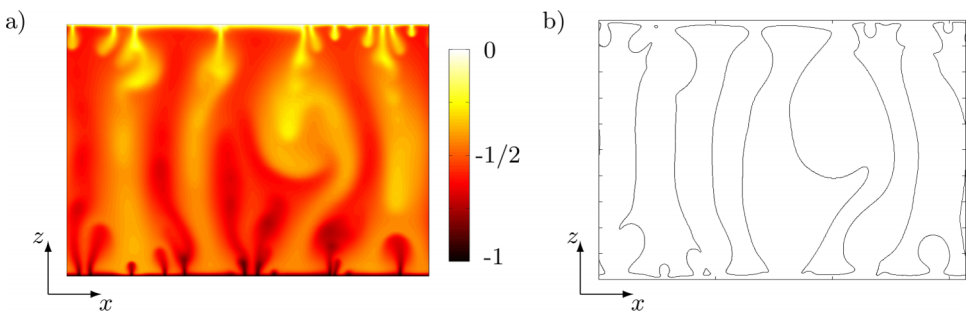

FIG. 8. (a): contour maps of the concentration field C in the entire domain. Dark regions indicate small solute concentration (light fluid) whereas bright regions indicates large solute concentration (heavy fluid). (b): corresponding shape of plumes identified by the present plume-detection algorithm, i.e., by detecting the contour line $C(\mathbf{x}) = -1/2$.

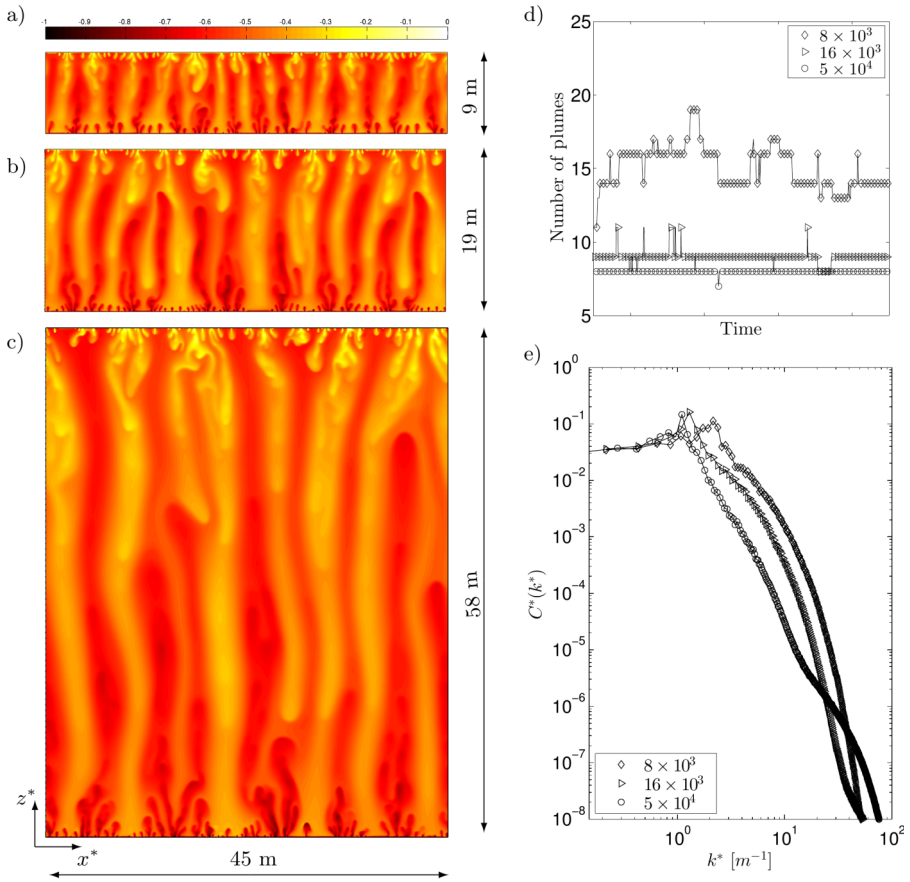

FIG. 9. Plume statistics for the isotropic case ($\gamma = 1$) and for three different Ra number. (a)–(c): instantaneous distribution of the concentration fields at $Ra = 8\times10^3, 16\times10^3$ and 5×10^4. (d): number of plumes computed in time (along the half-channel height) using the present plume detection algorithm. (e): power spectra of the concentration C for the three different Rayleigh-Darcy number analyzed here as a function of the physical wavenumber $k^* = 2\pi n/L^*$.

2. Plume statistics

Upon identification of a plume, we are able to compute their number, width and extension (surface area). Plume statistics computed at different Ra and for the isotropic case ($\gamma = 1$) are given in Fig. 9: in the left column (Figs. 9(a)–9(c)), we show contour maps of solute concentration in the entire domain (whose size is here expressed in dimensional units, [m]) for $Ra = 8 \times 10^3$ (Fig. 9(a)), $Ra = 16 \times 10^3$ (Fig. 9(b)) and $Ra = 5 \times 10^4$ (Fig. 9(c)). The values of H^* and L^* have been chosen to mimick a realistic physical situations. Hence, H^* ranges between 9 and 58 m whereas $L^* = 45$ m. The time evolution of the number of megaplumes (detected along the centerline of the channel, $z^* = H^*/2$, using the plume detection algorithm presented above) for the three different cases is presented in Fig. 9(d). Increasing Ra has a twofold effect on megaplumes: it decreases their number while increasing their persistence. This is clearly visible from the variability of the number of megaplumes in time, which is highly fluctuating for $Ra = 8 \times 10^3$, whereas it is almost constant for $Ra = 5 \times 10^4$. Note also that, since the physical domain is kept constant for varying Ra ($L_x^* = 45.562$ m), a reduction in the number of plumes (at large Ra) reflects into an increase in the average plume diameter. Results, not shown here for brevity, indicate that the average plume diameter is 1.5 m for $Ra = 8 \times 10^3$, 2.4 m for $Ra = 16 \times 10^3$, and 2.8 m for $Ra = 5 \times 10^4$. A more quantitative estimate of the number of megaplumes can be obtained by looking at the power spectra of the concentration field computed along the centerline of the channel, as shown in Fig. 9(e). The wavenumber (k^*_{max}) at which the power spectrum has a maximum is linked to the number of megaplumes in the cell. In particular, we found that $k^*_{max} = 2.15$ m^{-1} for $Ra = 8 \times 10^3$,

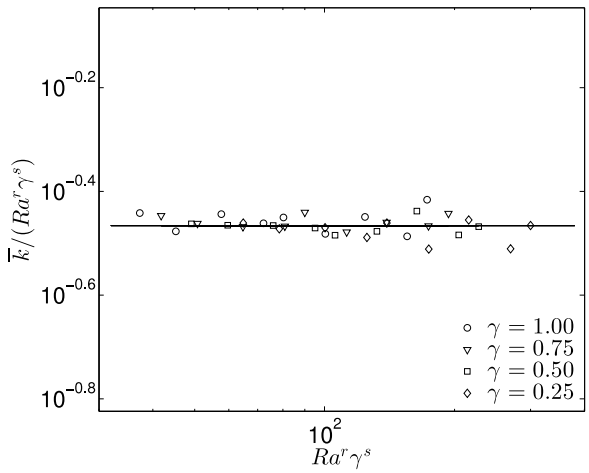

FIG. 10. Horizontally averaged wavenumbers $\overline{k}$ obtained from our numerical simulations at different Rayleigh-Darcy numbers Ra and different permeability ratios γ (symbols). Results are normalized by Ra^r and γ^s. An analytical scaling with $r = 0.48$ and $s = -0.40$ (straight line) is presented for comparison purposes.

$k^*_{max} = 1.29$ m^{-1} for $Ra = 16 \times 10^3$ and $k^*_{max} = 1.10$ m^{-1} for $Ra = 5 \times 10^4$. From the wavenumber definition $k^*_{max} = 2\pi n/L^*$, we can therefore evaluate n, here identifying the number of megaplumes, for the three different cases. We obtain $n \simeq 15$ for $Ra = 8 \times 10^3$, $n \simeq 9$ for $Ra = 16 \times 10^3$, and $n \simeq 8$ for $Ra = 5 \times 10^4$, in agreement with the value of n inferred from the qualitative plume detection (see Fig. 9(d)). From the knowledge of the concentration power spectrum $C(k)$, we can compute, at each time instant t_j, the average horizontal wavenumber k_j as

$$k_j = \frac{\int kC(k)dk}{\int C(k)dk}. \tag{16}$$

The instantaneous values of the wavenumber k_j are then averaged also in time to give the dimensionless average wavenumber $\overline{k}$. We perform this calculation for both isotropic ($\gamma = 1$) and non-isotropic permeability ($\gamma < 1$). From our numerical measurements (Fig. 10), we found

$$\overline{k} = 0.342 Ra^{0.48}\gamma^{-0.40}, \tag{17}$$

which is in fair agreement with the predictions given for the isotropic case[3] $\overline{k} = 0.48 Ra^{0.4}$. The slight discrepancy between the results could be possibly due to a difference in the cell dimension (see the Appendix).

IV. RELATIONSHIP BETWEEN THE TWO-SIDED AND THE ONE-SIDED CELL

To analyze the physics of concentration-driven CO_2 dissolution in geological reservoirs, the adoption of the so-called one-sided cell is perhaps more indicated compared to the two-sided cell discussed above. Differently from the two-sided cell, in the one-sided cell, convection occurs only from the upper boundary whereas the lower boundary is an impenetrable and no-flux boundary. Details on the different boundary conditions characterizing the two-sided and the one-sided cell are given in Fig. 11.

In the literature, the transient solute dynamics in the one-sided cell has been recently analyzed experimentally[27] and numerically[12,13,28] for isotropic porous media. The characteristic dynamics of the one-sided cell is the following. After injection of solute from the upper boundary, diffusion dominates until fingers become strong enough to trigger vertical convective motions. Fingers become stronger and stronger in time and merge into large and columnar plumes (megaplumes) that extend vertically over the entire domain. Once megaplumes reach the bottom boundary, the domain starts filling with dense solute. This is the final (and longer) stage of the entire process of solute convection, and is usually called the "shutdown regime." As already discussed for the case of isotropic porous media,[12,23] during the shutdown regime a precise connection between the two-sided

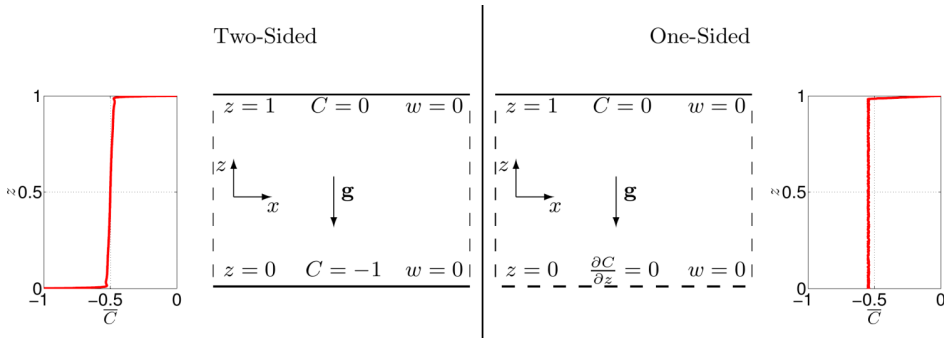

FIG. 11. Sketch of the computational domain in the two-sided (left panel) and in the one-sided (right panel) cell. The two-sided cell (left) has physical boundaries, characterized by an imposed value of the solute concentration, in the vertical direction (upper and lower horizontal solid lines), whereas it has periodic boundaries in the horizontal direction (left and right vertical dashed lines). The one-sided cell (right) is instead characterized by a zero-flux boundary condition at the lower boundary (impenetrable and no-flux condition).

and the one-sided cell can be established. In the following, we will try to extend this link also in case of anisotropic porous media.

The one-sided cell corresponds to one half of the two-sided cell. In particular, it is characterized by a cell height and by a density difference both of which is one-half of the corresponding value of the two-sided cell. As a consequence, indicating with Ra_1 and Ra_2 the Rayleigh-Darcy numbers of the one-sided cell and of the two-sided cell respectively, we have $Ra_2 = 4Ra_1$.

We start from the theoretical box model proposed by Hewitt *et al.*[12] and we try to extend it to the case of anisotropic porous media. The solute flux in the one-sided cell is conveniently defined as

$$F(t) = \frac{1}{L}\int_0^L \left.\frac{\partial C(x,t)}{\partial z}\right|_{z=1} dx, \tag{18}$$

while the mean concentration at time t and at the vertical position z is

$$\overline{C}(z,t) = \frac{1}{L}\int_0^L C(z,t)dx. \tag{19}$$

Following the work of Hewitt *et al.*,[12] we assume the following: (i) far from the walls, the averaged concentration profile is uniform over the domain height $\overline{C}(z,t) \approx \overline{C}(t) = \vartheta(t)$; (ii) during the shut-down regime, the fundamental flow structures are those that characterize the steady-state two-sided system (protoplumes and megaplumes); and (iii) the Rayleigh-Darcy number in the one-sided domain, defined as $Ra = gH^*K_v\Delta\rho^*/(\mu\phi D)$, depends on the actual density difference $\Delta\rho^*$ existing between the top of the domain and a generic point outside the boundary layer. Under the above hypotheses, it is possible to define a time-dependent Rayleigh-Darcy number, $Ra(t) = Ra_0|\vartheta(t)|$, where Ra_0 is computed based on the initial density difference.

We consider the time-dependent three dimensional advection-diffusion equation

$$\frac{\partial C}{\partial t} + \mathbf{u}\cdot\nabla C = \frac{1}{Ra_0}\left[\gamma\left(\frac{\partial^2 C}{\partial x^2} + \frac{\partial^2 C}{\partial y^2}\right) + \frac{\partial^2 C}{\partial z^2}\right] \tag{20}$$

and we integrate it over the whole domain. Imposing the boundary conditions

$$w = 0, \quad \frac{\partial C}{\partial z} = 0 \quad \text{on} \quad z = 0, \tag{21}$$

$$w = 0, \quad C = 0 \quad \text{on} \quad z = 1 \tag{22}$$

and using the Stokes theorem and definition (19), we obtain

$$\frac{\partial}{\partial t}\int_0^1 \overline{C}(z,t)\,dz = \frac{1}{Ra_0}\frac{1}{L}\int_0^L \left.\frac{\partial C}{\partial z}\right|_{z=1} dx. \tag{23}$$

Assuming that the averaged concentration profile is uniform over the vertical direction z, we have $\overline{C}(z,t) \approx \vartheta(t)$. As a result, the left-hand side of Eq. (23) reduces to

$$\frac{\partial}{\partial t}\int_0^1 \overline{C}(z,t)\,dz \approx \frac{\partial}{\partial t}\int_0^1 \vartheta(t)\,dz = \frac{\partial \vartheta(t)}{\partial t}. \tag{24}$$

Note that the same result can be obtained also considering two lateral impermeable walls (in the x direction) instead of two periodic boundaries. According to the Nusselt number definition adopted for the one-sided domain (see the Appendix), we finally obtain the evolution in time of the solute concentration,

$$\frac{d\vartheta(t)}{dt} = \frac{Nu(t)}{Ra_0}|\vartheta(t)|. \tag{25}$$

To resolve Eq. (25) we need an estimate for $Nu(t)$ in case of anisotropic porous media. This is accomplished here using our previous predictions (correlation (15)) with the modified Rayleigh number $Ra = 4Ra_0$ (to switch from the one-sided to the two-sided cell).

By imposing the initial condition $\vartheta(t_0 = 0) = -1$, we obtain the time behaviour of the mean concentration profile,

$$\vartheta(t) = \frac{\beta}{4Ra_0\gamma^n\alpha}\left[1 - \left(1 + \frac{\beta}{4Ra_0\gamma^n\alpha}\right)\exp\left(\frac{\beta}{Ra_0}t\right)\right]^{-1}. \tag{26}$$

Upon definition of $\varepsilon = \beta/(4Ra_0\gamma^n\alpha)$, we have

$$\vartheta(t) = \varepsilon\left[1 - (1+\varepsilon)\exp(4\alpha\gamma^n\varepsilon t)\right]^{-1}. \tag{27}$$

In the limit of large Ra, $\varepsilon \to 0$ and we finally get the following expression for the time behaviour of the mean concentration profile and of the vertical flux as a function of the permeability ratio γ:

$$\vartheta(\gamma,t) \approx \frac{-1}{1 + 4\alpha\gamma^n t}, \tag{28}$$

$$F(\gamma,t) \approx \frac{4\alpha\gamma^n Ra_0}{\left[1 + 4\alpha\gamma^n t\right]^2}. \tag{29}$$

Note that, for $Ra = 10^4$, the difference between the prediction given by Eq. (27) and by Eq. (28) is always below 1% of the maximum value of $\vartheta(t)$, which makes the approximation $\varepsilon \to 0$ reasonable for solute convection in real-scale reservoirs.

The behaviour of $F(\gamma,t)$ for the different values of γ considered in this study is shown in Fig. 12(a). At the beginning, $F(\gamma,t)$ is larger for smaller γ, indicating that the vertical flux of solute increases for decreasing γ. At later stages, we observe a crossover between the different curves occurring at $t = \tilde{t}$. By matching the value of $F(\gamma,t)$ for two different values of γ (here indicated by γ_1 and γ_2), we obtain the value of the crossover time $\tilde{t} = (\gamma_1\gamma_2)^{-n/2}/4\alpha$, which falls in the range $\tilde{t} = [30; 35]$ and is only slightly sensitive to the value of γ.

From the knowledge of the instantaneous solute flux $F(\gamma,t)$ we can explicitly compute, for a given γ, the total amount of solute $\mathcal{F}(\gamma,t)$ dissolved in the entire domain during the shutdown regime,

$$\mathcal{F}(\gamma,t) = \frac{4\alpha\gamma^n t}{1 + 4\alpha\gamma^n t}Ra_0. \tag{30}$$

In particular, we consider the time behaviour of the normalized difference $(\mathcal{F}(\gamma,t) - \mathcal{F}(1,t))/(\mathcal{F}(1,t))$ between the solute dissolved for $\gamma \neq 1$ and that dissolved for $\gamma = 1$. Results, which are shown in Fig. 12(b), indicate that during the initial transient, the quantity of solute dissolved for $\gamma = 0.25$ can be 40% larger than that for $\gamma = 1$. This suggests that, for finite times, the amount of solute that can be efficiently dissolved in real reservoirs ($\gamma \neq 1$) is considerably larger compared to the uniform permeability case ($\gamma = 1$). As expected, in the long-term limit we have $\mathcal{F}(t \to +\infty) \to Ra_0$, which means that for extremely long times the amount of dissolved solute depends only on the available volume (Ra_0) but not on γ. Note however that this result is not in contrast with the previous observation that for finite times ($t^* < 10^2$ yr) γ has a strong impact on the amount of dissolved solute.

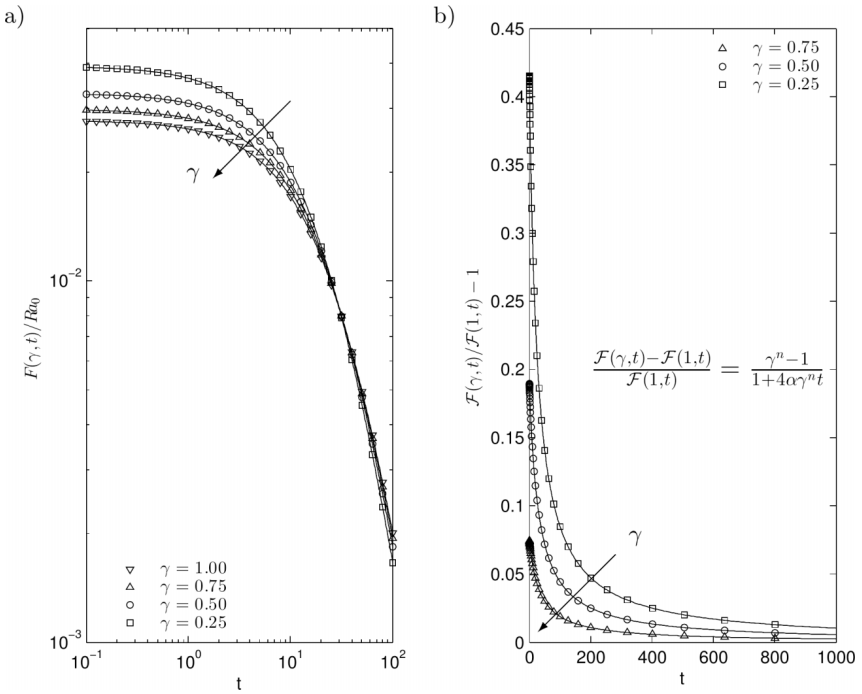

FIG. 12. (a): time behaviour of the vertical solute flux ($F(\gamma,t)/Ra_0$, see also Eq. (29)) computed for a one-sided domain for different values of γ. (b): time behaviour of the normalized amount of solute (30) for different values of γ.

V. CONCLUSIONS AND FUTURE DEVELOPMENTS

Solute convection in porous media at high Rayleigh-Darcy number Ra is characterized by complex macroscopic phenomena (viscous fingering, megaplumes) that are difficult to model and to predict. Further complications arise when the porous medium is non-isotropic. This is the case of realistic sedimentary rock reservoirs, which can be modelled as porous media with a vertical-to-horizontal permeability ratio $\gamma = K_v/K_h$ smaller than unity.

In this paper we focused exactly on the effect of γ (with $\gamma < 1$) on the solute convection in a two-dimensional saturated porous medium. We started considering the case of the so-called two-sided domain, in which convective transport occurs between a lighter layer (lower boundary) and a heavier layer (upper boundary). We performed simulations for a range of Rayleigh-Darcy numbers Ra ranging from 50 to 5×10^4. We have characterized the flow dynamics in terms of protoplumes (small plumes emerging from the boundary) and megaplumes (generated by the coalescence of protoplumes). Flow field statistics obtained for different Ra and different γ have been compared to discuss the role of the different parameters on the overall transport efficiency of the solute. We have shown that, for $\gamma < 1$, the vertical convective flux of solute increases significantly (up to 40%, for the range of γ examined here). We have also linked this phenomenon to the modification of the flow topology: increasing K_h (i.e., decreasing γ) increases the horizontal velocity gradient of the saturated fluid and in turn enhances the solute vertical transport.

We finally used our results on the two-sided configuration to introduce and discuss the solute dynamics in the so-called one-sided configuration (where convection occurs only away from the upper boundary). This configuration is perhaps more related to the physics of the concentration driven CO_2 dissolution process. We found that, for realistic CO_2 dumping times ($t^* < 10^2$ yr), the amount of CO_2 that can be efficiently dissolved in sedimentary rock reservoirs characterized by $\gamma < 1$ is larger than that dissolved in case of $\gamma = 1$ (isotropic porous medium). This result opens new intriguing perspectives on the efficiency of long-term geological CO_2 storage.

A. Implication for CO_2 sequestration

In the following, we will try to put the results presented above in the context of CO_2 sequestration in real reservoirs. We consider the case of Sleipner site, in the North Sea. We assume[23,29] a porous medium with uniform porosity $\phi = 0.3$, vertical permeability $K_v = 3 \times 10^{-12}$ m^2 and a layer depth $H^* = 20$ m. The thermophysical properties of the fluid are those of CO_2 + brine at a depth of 1 km (typical reservoir location). In particular, Pau *et al.*[30] suggested a top-to-bottom density difference $\Delta\rho^* = 10.45$ kg/m^3, viscosity $\mu = 595 \times 10^{-6}$ Pa × s and diffusivity $D = 2 \times 10^{-9}$ m^2/s. The resulting Rayleigh-Darcy number is $Ra \approx 17 \times 10^3$. The free-fall buoyancy velocity and the convective time scale are $W^* \approx 16.3$ m/yr and $\hat{t} = \phi H^*/W^* \approx 0.37$ yr, respectively.

From Eq. (29), we derive the dimensional value of the convective flux F^*, in terms of the physical time t^* and anisotropic permeability ratio γ,

$$F^*(\gamma, t^*) = \frac{4\alpha\gamma^n \hat{t}}{\left[\hat{t} + 4\alpha\gamma^n t^*\right]^2} H^* \phi C_s^*. \tag{31}$$

The total amount of CO_2 dissolved during the shutdown regime, see Eq. (30), is

$$\mathcal{F}^*(\gamma, t^*) = \frac{4\alpha\gamma^n t^*}{\hat{t} + 4\alpha\gamma^n t^*} H^* \phi C_s^*. \tag{32}$$

In Fig. 13 we report, for the present example, the convective fluxes and the dissolved CO_2 for the two extreme cases of $\gamma = 1$ (isotropic medium) and $\gamma = 0.25$. Results clearly show that, up to the critical time $\widetilde{t^*} \approx 11.2$ yr, the convective flux of CO_2 (Fig. 13(a)) is definitely larger for $\gamma = 0.25$ than for $\gamma = 1$ (isotropic case). This reflects into a larger amount of dissolved CO_2 for $t^* < 10^3$ (Fig. 13(b)). Alternatively, we might say that, for a given amount of CO_2 per unit area $\overline{\mathcal{F}^*}$ to be injected beneath the earth surface, the dissolution time for safety CO_2 storage is definitely shorter when $\gamma < 1$. To put some numbers, if $\overline{\mathcal{F}^*} = 150$ kg/m^2, the dissolution times are $t^* = 10$ yr for $\gamma = 0.25$ and $t^* = 15$ yr for $\gamma = 1$. Note also that, for extremely long times ($t^* \to \infty$), the amount of dissolved CO_2, is independent of γ, and is roughly 3×10^2 kg/m^2. This represents indeed a theoretical estimate of the overall storage capability of the reservoir.

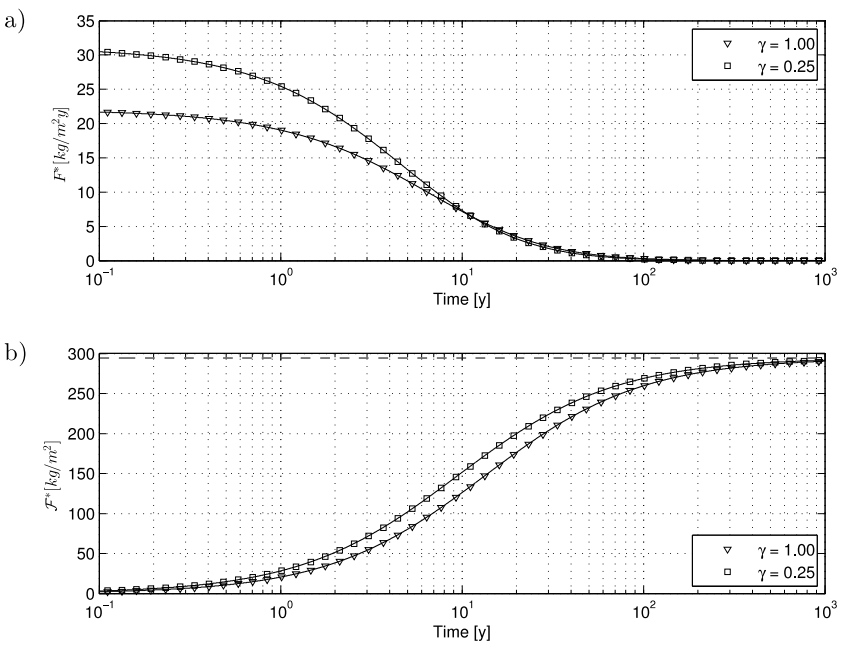

FIG. 13. CO_2 convective flux (a) and total CO_2 dissolved (b) in time. Dashed line represents the maximum amount of CO_2 dissoluble per unit area.

ACKNOWLEDGMENTS

The authors acknowledge CINECA Supercomputing Center for the availability of high performance computing resources and support.

APPENDIX: COMPUTATIONAL DETAILS

In this section, we report some details on the numerical methodology employed in the present study.

1. Details on the numerical approach

We used a pseudo-spectral method, which transforms field variables in the wavenumber space through a Discrete Fourier Transform in the horizontal direction and a Chebyshev expansion in the wall-normal direction.[31] Equations (10)-(12) are rewritten in vectorial form as

$$\mathbf{u} = -\nabla P + \mathbf{k}C, \tag{A1}$$

$$\nabla \cdot \mathbf{u} = 0, \tag{A2}$$

$$\frac{DC}{Dt} = \frac{1}{Ra}\left(\gamma \nabla_H^2 C + \frac{\partial^2 C}{\partial z^2}\right), \tag{A3}$$

with $\mathbf{k}$ the unit vector in the vertical direction and $\nabla_H^2 = \frac{\partial^2}{\partial x^2} + \frac{\partial^2}{\partial y^2}$. Taking twice the curl of (A1) and using (A2), it is possible to compute the wall-normal velocity $\hat{w}$ by solving a second order Helmholtz equation in the wavenumber space (k_x, k_y),

$$\left[\frac{\partial^2}{\partial z^2} - \left(k_x^2 + k_y^2\right)\right]\hat{w} = -\left(k_x^2 + k_y^2\right)C. \tag{A4}$$

Once $\hat{w}$ is available, $\hat{u}$ and $\hat{v}$ can be determined as

$$\hat{u} = i\frac{k_x}{k_x^2 + k_y^2}\frac{\partial \hat{w}}{\partial z}, \tag{A5}$$

$$\hat{v} = i\frac{k_y}{k_x^2 + k_y^2}\frac{\partial \hat{w}}{\partial z}. \tag{A6}$$

Equation (A3) is then discretized in time using an Adams-Bashforth explicit method for the non-linear term $S = \mathbf{u} \cdot \nabla C$ and a Crank-Nicholson implicit method for the diffusive term,

$$\frac{\hat{C}^{n+1} - \hat{C}^n}{\Delta t} = \frac{3}{2}\hat{S}^n - \frac{1}{2}\hat{S}^{n-1} + \frac{1}{2Ra}\left(\gamma \nabla_H^2 + \frac{\partial^2}{\partial z^2}\right)\left(\hat{C}^{n+1} - \hat{C}^n\right). \tag{A7}$$

The computational time step Δt has been chosen to fulfill the CFL condition and ranges between $\Delta t = 2 \times 10^{-3}$ ($Ra = 2 \times 10^3$ and $\gamma = 1$) and $\Delta t = 5 \times 10^{-5}$ ($Ra = 5 \times 10^4$ and $\gamma = 0.25$).

Transforming (A7) in the wavenumber space, the concentration $\hat{C}$ can be obtained by solving the second order Helmholtz equation,

$$\left(\frac{\partial^2}{\partial z^2} - \frac{1 + \gamma\delta(k_x^2 + k_y^2)}{\delta}\right)\hat{C}^{n+1} = -\frac{\hat{H}}{\delta}, \tag{A8}$$

where $\delta = \frac{\Delta t}{2Ra}$ and

$$\hat{H} = \delta\left(\frac{\partial^2}{\partial z^2} - \frac{1 + \gamma\delta(k_x^2 + k_y^2)}{\delta}\right)\hat{C}^n + \delta Ra\left(3\hat{S}^n - \hat{S}^{n-1}\right). \tag{A9}$$

The initial condition of the present simulations consists of a perturbed linear concentration profile,

$$C_0(z) = C(0) + \left[C(1) - C(0)\right]z + \xi \tag{A10}$$

where $C(0)$ and $C(1)$ are the values of the concentration at the bottom and top walls whereas ξ is a random number with amplitude $|\xi| < 2 \times 10^{-3}|C(1) - C(0)|$.

Following the work of Wen *et al.*,[32] and considering that the horizontal scales become thinner in high-Ra convection in porous media, we ran simulations on a domain whose aspect ratio $\Gamma = L/H$ was reduced from 2π to $\pi/4$ for increasing Ra. The resulting domain was discretized in space using up to 8192×1025 nodes in the x and z directions for $Ra = 5 \times 10^4$. We finally checked that the steady state solution was independent of the spatial resolution (grid independence) and of the aspect ratio Γ.

2. Details on the Nusselt number calculation

The Nusselt number Nu, which represents the non-dimensional flux of heat or solute through the boundaries of a two-sided domain, is computed as

$$\overline{Nu}(t) = \frac{1}{2L}\int_0^L \left(\frac{\partial C(x,t)}{\partial z}\bigg|_{z=0} + \frac{\partial C(x,t)}{\partial z}\bigg|_{z=1} \right) dx. \tag{A11}$$

Note that the Nusselt number, averaged in space over the horizontal direction x, is a function of time. However, after an initial transient t_i, the simulation reaches a steady state condition (whose final instant is t_f), where the Nusselt number fluctuates around an asymptotic value $\langle Nu \rangle$ evaluated as

$$\langle Nu \rangle = \frac{1}{t_f - t_i}\int_{t_i}^{t_f} \overline{Nu}(t)\, dt. \tag{A12}$$

Throughout the paper, $\langle Nu \rangle$ is indicated as Nu for ease of reading. Statistics are averaged over a time window of $150 \times \hat{t}$, where $\hat{t}$ is the convective time scale $\hat{t} = \phi H^*/W^*$ (with ϕ the porosity, H^* the domain height and W^* the freefall buoyancy velocity). Note that for the one-sided configuration, we defined the time-dependent Nusselt number $Nu(t)$ following Hewitt *et al.*[12] as

$$Nu(t) = \frac{F(t)}{|\vartheta(t)|}, \tag{A13}$$

where $F(t)$ is the solute flux and $\vartheta(t)$ is the concentration difference.

[1] C. W. Horton and F. T. Rogers, Jr., "Convection currents in a porous medium," J. Appl. Phys. **16**(6), 367–370 (1945).
[2] E. R. Lapwood, "Convection of a fluid in a porous medium," Proc. Cambridge **44**, 508–521 (1948).
[3] D. R. Hewitt, J. A. Neufeld, and J. R. Lister, "Ultimate regime of high Rayleigh number convection in a porous medium," Phys. Rev. Lett. **108**(22), 224503 (2012).
[4] J. Otero, L. A. Dontcheva, H. Johnston, R. A. Worthing, A. Kurganov, G. Petrova, and C. R. Doering, "High-Rayleigh number convection in a fluid-saturated porous layer," J. Fluid Mech. **500**, 263–281 (2004).
[5] S. Backhaus, K. Turitsyn, and R. E. Ecke, "Convective instability and mass transport of diffusion layers in a Hele-Shaw geometry," Phys. Rev. Lett. **106**(10), 104501 (2011).
[6] G. J. Weir, S. P. White, and W. M. Kissling, "Reservoir storage and containment of greenhouse gases," Transp. Porous Media **23**(1), 37–60 (1996).
[7] H. E. Huppert and J. A. Neufeld, "The fluid mechanics of carbon dioxide sequestration," Annu. Rev. Fluid Mech. **46**, 255–272 (2014).
[8] B. Metz, O. Davidson, H. de Coninck, M. Loos, L. Meyer *et al.*, Carbon dioxide capture and storage: Special report of the IPCC, 2005.
[9] D. P. Schrag, "Preparing to capture carbon," Science **315**(5813), 812–813 (2007).
[10] S. Julio Friedmann, "Geological carbon dioxide sequestration," Elements **3**(3), 179–184 (2007).
[11] X. Xu, S. Chen, and D. Zhang, "Convective stability analysis of the long-term storage of carbon dioxide in deep saline aquifers," Adv. Water Res. **29**(3), 397–407 (2006).
[12] D. R. Hewitt, J. A. Neufeld, and J. R. Lister, "Convective shutdown in a porous medium at high Rayleigh number," J. Fluid Mech. **719**, 551–586 (2013).
[13] A. C. Slim, "Solutal-convection regimes in a two-dimensional porous medium," J. Fluid Mech. **741**, 461–491 (2014).
[14] A. Riaz, M. Hesse, H. A. Tchelepi, and F. M. Orr, "Onset of convection in a gravitationally unstable diffusive boundary layer in porous media," J. Fluid Mech. **548**, 87–111 (2006).
[15] P. Cheng, M. Bestehorn, and A. Firoozabadi, "Effect of permeability anisotropy on buoyancy-driven flow for CO_2 sequestration in saline aquifers," Water Resour. Res. **48**(9), 1–16, doi:10.1029/2012WR011939 (2012).
[16] J. Ennis-King, I. Preston, and L. Paterson, "Onset of convection in anisotropic porous media subject to a rapid change in boundary conditions," Phys. Fluids (1994-present) **17**(8), 084107 (2005).

[17] A. J. Landman and R. J. Schotting, "Heat and brine transport in porous media: The Oberbeck-Boussinesq approximation revisited," Transp. Porous Media **70**(3), 355–373 (2007).
[18] D. R. Hewitt, J. A. Neufeld, and J. R. Lister, "Stability of columnar convection in a porous medium," J. Fluid Mech. **737**, 205–231 (2013).
[19] F. Zonta and A. Soldati, "Effect of temperature dependent fluid properties on heat transfer in turbulent mixed convection," J. Heat Transfer **136**(2), 022501 (2014).
[20] M. D. Graham and P. H. Steen, "Plume formation and resonant bifurcations in porous-media convection," J. Fluid Mech. **272**, 67–90 (1994).
[21] J. Schumacher, "Lagrangian studies in convective turbulence," Phys. Rev. E **79**(5), 056301 (2009).
[22] C. P. Green and J. Ennis-King, "Steady dissolution rate due to convective mixing in anisotropic porous media," Adv. Water Resour. **73**, 65–73 (2014).
[23] J. A. Neufeld, M. A. Hesse, A. Riaz, M. A. Hallworth, H. A. Tchelepi, and H. E. Huppert, "Convective dissolution of carbon dioxide in saline aquifers," Geophys. Res. Lett. **37**(22), 1–5, doi:10.1029/2010GL044728 (2010).
[24] F. Paparella and J. von Hardenberg, "Clustering of salt fingers in double-diffusive convection leads to staircaselike stratification," Phys. Rev. Lett. **109**(1), 014502 (2012).
[25] E. S. C. Ching, H. Guo, X.-D. Shang, P. Tong, and K.-Q. Xia, "Extraction of plumes in turbulent thermal convection," Phys. Rev. Lett. **93**(12), 124501 (2004).
[26] E. P. van der Poel, R. Verzicco, S. Grossmann, and D. Lohse, "Plume emission statistics in turbulent Rayleigh–Bénard convection," J. Fluid Mech. **772**, 5–15 (2015).
[27] A. C. Slim, M. M. Bandi, J. C. Miller, and L. Mahadevan, "Dissolution-driven convection in a Hele–Shaw cell," Phys. Fluids (1994-present) **25**(2), 024101 (2013).
[28] J. J. Hidalgo, J. Fe, L. Cueto-Felgueroso, and R. Juanes, "Scaling of convective mixing in porous media," Phys. Rev. Lett. **109**(26), 264503 (2012).
[29] M. Bickle, A. Chadwick, H. E. Huppert, M. Hallworth, and S. Lyle, "Modelling carbon dioxide accumulation at Sleipner: Implications for underground carbon storage," Earth Planet. Sci. Lett. **255**(1), 164–176 (2007).
[30] G. S. H. Pau, J. B. Bell, K. Pruess, A. S. Almgren, M. J. Lijewski, and K. Zhang, "High-resolution simulation and characterization of density-driven flow in CO_2 storage in saline aquifers," Adv. Water Resour. **33**(4), 443–455 (2010).
[31] F. Zonta, C. Marchioli, and A. Soldati, "Modulation of turbulence in forced convection by temperature-dependent viscosity," J. Fluid Mech. **697**, 150–174 (2012).
[32] B. Wen, G. P. Chini, N. Dianati, and C. R. Doering, "Computational approaches to aspect-ratio-dependent upper bounds and heat flux in porous medium convection," Phys. Lett. A **377**(41), 2931–2938 (2013).